The Role of Seasonality and the ENSO Mode in Central and East Pacific ENSO Growth and Evolution

DANIEL J. VIMONT,[a,b] MATTHEW NEWMAN,[c,d] DAVID S. BATTISTI,[e] AND SANG-IK SHIN[c,d]

[a] *Nelson Institute Center for Climatic Research, University of Wisconsin–Madison, Madison, Wisconsin*
[b] *Atmospheric and Oceanic Sciences Department, University of Wisconsin–Madison, Madison, Wisconsin*
[c] *Cooperative Institute for Research in Environmental Sciences, University of Colorado Boulder, Boulder, Colorado*
[d] *NOAA/Physical Sciences Laboratory, Boulder, Colorado*
[e] *Department of Atmospheric Sciences, University of Washington, Seattle, Washington*

ABSTRACT: A cyclostationary linear inverse model (CSLIM) is used to investigate the seasonal growth of tropical Pacific Ocean El Niño–Southern Oscillation (ENSO) events with canonical, central Pacific (CP), or eastern Pacific (EP) sea surface temperature (SST) characteristics. Analysis shows that all types of ENSO events experience maximum growth toward final states occurring in November and December. ENSO events with EP characteristics also experience growth into May and June, but CP events do not. A single dominant "ENSO mode," growing from an equatorial heat content anomaly into a characteristic ENSO-type SST pattern in about 9 months (consistent with the delayed/recharge oscillator model of ENSO), is essential for the predictable development of all ENSO events. Notably, its seasonality is responsible for the late-calendar-year maximum in ENSO amplification. However, this ENSO mode alone does not capture the observed growth and evolution of diverse ENSO events, which additionally involve the seasonal evolution of other nonorthogonal Floquet modes. EP event growth occurs when the ENSO mode is initially "covered up" in combination with other Floquet modes. The ENSO mode's slow seasonal evolution allows it to emerge while the other modes rapidly evolve and/or decay, leading to strongly amplifying and more predictable EP events. CP events develop when the initial state has a substantial contribution from Floquet modes with meridional mode–like SST structures. Thus, while nearly all ENSO events involve the seasonally varying ENSO-mode dynamics, the diversity and predictability of ENSO events cannot be understood without identifying contributions from the remaining Floquet modes.

SIGNIFICANCE STATEMENT: The purpose of this study is to identify structures that lead to seasonal growth of diverse types of El Niño–Southern Oscillation (ENSO) events. An important contribution from this study is that it uses an observationally constrained, empirically derived seasonal model. We find that processes affecting the evolution of diverse ENSO events are strongly seasonally dependent. ENSO events with eastern equatorial Pacific sea surface temperature (SST) characteristics are closely related to a single "ENSO mode" that resembles theoretical models of ENSO variability. ENSO events that have central equatorial Pacific SST characteristics include contributions from additional "meridional mode" structures that evolve via different physical processes. These findings are an important step in evaluating the seasonal predictability of ENSO diversity.

1. Introduction

Interannual variability associated with the tropical Pacific El Niño–Southern Oscillation (ENSO) phenomenon is the dominant form of year-to-year variability in the climate system, with important contributions to seasonal predictability that extend far outside of the tropical Pacific (Rasmusson and Carpenter 1982; Ropelewski and Halpert 1987; Wallace et al. 1998; Barnston et al. 2010; Chen and Wallace 2015; Newman and Sardeshmukh 2017; Lenssen et al. 2020). "Canonical" ENSO events evolve via relatively well-established dynamics

that involve coupling between equatorial sea surface temperature (SST), thermocline depth, and atmospheric surface winds (see Neelin et al. 1998; Battisti et al. 2019, for reviews). The relative importance of these processes varies from event to event and throughout the seasonal cycle, leading to inter-event differences and a seasonal ENSO evolution with events tending to peak toward the end of the calendar year (Rasmusson and Carpenter 1982; Wallace et al. 1998; Larkin and Harrison 2002). This seasonality also extends to the seasonality of ENSO prediction skill (Balmaseda et al. 1995; Torrence and Webster 1998; Jin et al. 2008; Wu et al. 2009; Newman and Sardeshmukh 2017; Jin et al. 2019), which tends to drop off rapidly as forecast initialization is pushed earlier in boreal spring.

Early studies of ENSO dynamics (Zebiak and Cane 1987; Battisti 1988) used "intermediate" models that simulated ocean–atmosphere interactions around a prescribed annual

---

⊘ Denotes content that is immediately available upon publication as open access.

Corresponding author: Daniel J. Vimont, dvimont@wisc.edu

cycle (see Battisti et al. 2019, for a review). In those models ENSO variance was maintained via a self-sustaining (linearly unstable) "ENSO mode" that reproduced fundamental characteristics of ENSO variability including the spatial structure, interannual time scale, phase-locking to the seasonal cycle, and some ability to predict ENSO in nature. Penland and Sardeshmukh (1995) highlighted a different paradigm for understanding ENSO variance and irregularity through the use of an empirically derived "linear inverse model" (LIM). In this paradigm ENSO growth and evolution occurs via a set of nonorthogonal, linearly damped modes where a stable ENSO mode is initially "covered up" by other, more rapidly evolving eigenmodes (see also Newman et al. 2011a). ENSO variance and irregularity are ultimately maintained by (relatively) fast phenomena that are parameterized as a stochastic forcing (Penland and Matrosova 1994). In their non–seasonally varying model, ENSO phase locking was thought to be a consequence of seasonality in the stochastic forcing (Penland 1996) rather than due to seasonal evolution of the ENSO mode(s). Using a similar method, Johnson et al. (2000a,b) derived a cyclostationary Markov model and demonstrated an important role for seasonality in the empirical operator; Thompson and Battisti (2001) showed the same in a linearized version of the seasonally varying Zebiak and Cane (1987) model. Shin et al. (2021) confirmed (and more) the findings of Johnson et al. (2000b) by developing a cyclostationary linear inverse model (CSLIM) using 20 years of additional (and improved subsurface) data. These empirically derived, seasonal models offer a new tool for investigating the seasonality of ENSO growth and evolution.

Under a linearly stable regime, external forcing is required to initiate and maintain ENSO variance. One source of stochastic forcing comes through the second most dominant source of ocean–atmosphere interaction in the Pacific, the "Pacific meridional mode" (PMM; Chiang and Vimont 2004). The PMM evolves via initial SST anomalies in the subtropics that propagate westward and equatorward via coupled ocean/atmosphere interactions that include a feedback between the surface wind, evaporation, and SST (the WES feedback; Xie and Philander 1994; Vimont 2010; Martinez-Villalobos and Vimont 2017). The PMM was identified after recognizing that midlatitude atmospheric variability can affect ENSO through the seasonal footprinting mechanism (SFM; Vimont et al. 2001, 2003a,b). Within the context of the SFM, the PMM acts as a conduit for connecting (stochastic) midlatitude variability to ENSO via evolving wind stress anomalies along the PMM's southern flank (Alexander et al. 2010; Thomas and Vimont 2016).

It is well established that ENSO events differ from one another in spatial and temporal evolution. In addition to more subtle, random differences, ENSO events can take on "central" or "east" Pacific (CP or EP, respectively) characteristics, as defined by the spatial structure of equatorial SST anomalies (Trenberth and Stepaniak 2001; Larkin and Harrison 2005; Ashok et al. 2007; Kao and Yu 2009; Kug et al. 2009; Capotondi et al. 2015). Vimont et al. (2014) investigate the growth of CP and EP ENSO variations using linear inverse modeling and show that the initial conditions that

optimize growth differ for EP and CP events. They find that off-equatorial SST anomalies associated with the PMM and SFM are important for initiating development of ENSO events with CP characteristics (Yu and Kim 2011; Newman et al. 2011b; Thomas et al. 2018). These CP-type events are less dependent on thermocline interactions (Vimont et al. 2014). In contrast, ENSO events with EP characteristics tend to be more sensitive to equatorial thermocline anomalies and off-equatorial SST anomalies in the Southern Hemisphere (Yu et al. 2011; Vimont et al. 2014; You and Furtado 2017). The differences in CP and EP dynamics and evolution affect seasonal prediction skill with CP-type events exhibiting less predictability than EP-type events (Zheng and Yu 2017; Hou et al. 2019).

This study aims to diagnose seasonal variations in growth of diverse ENSO structures, including those with CP or EP characteristics. This study expands on Vimont et al. (2014) by investigating the seasonality of growth rates and on Shin et al. (2021) by explicitly considering CP and EP structures. The paper is organized as follows: the LIM and CSLIM methods are described in section 2, and optimal growth and associated patterns are illustrated in section 3. Based on strong seasonality in ENSO growth rates, we isolate the impact of a single "ENSO mode" in section 4 to illustrate the role of modal versus transient growth in the evolution of ENSO events, including those with CP and EP characteristics. Section 5 reiterates the findings of the study and discusses some implications. While we include details of the analyses throughout the paper, we also note that such descriptions may be tedious for some readers and so provide summary interpretations of results at the beginning of sections 3 and 4.

2. Methods and data

a. Calculating the LIM or CSLIM

We use both a LIM and a CSLIM to investigate the structure and evolution of tropical Pacific Ocean variability. The LIM and CSLIM frameworks are described in more detail elsewhere (Penland and Sardeshmukh 1995; von Storch et al. 1995; Johnson et al. 2000b; Shin et al. 2021) but are briefly reviewed here. Both models assume that the slowly evolving (long time scale) dynamics of the tropical Pacific ocean/atmosphere system can be approximated as linear (including an implicit linear parameterization of the nonlinearities) and that on these longer time scales, the role of fast nonlinear processes can be approximated as Gaussian noise:

$$\frac{d\mathbf{x}}{dt} = \mathbf{L}\mathbf{x} + \xi, \tag{1}$$

where $\mathbf{x}$ is the system state vector (defined for this study below), $\mathbf{L}$ is the (potentially seasonally varying) linear dynamical feedback matrix, and ξ is the (spatially coherent) white noise forcing. This study does not consider the noise forcing [see Thomas et al. (2018) for a treatment of tropical Pacific noise forcing in a nonseasonal LIM]. For a standard "stationary" model, $\mathbf{L} \equiv \mathbf{L}^{ST}$ is constant in time and the homogeneous version of (1) yields the propagator $\mathbf{G}^{ST}(\tau)$:

$$\mathbf{x}(t + \tau) = \exp(\mathbf{L}^{ST}\tau)\mathbf{x}(t) \equiv \mathbf{G}^{ST}(\tau)\mathbf{x}(t) \cdot \quad (2)$$

Linear inverse modeling estimates the dynamical system matrix via first calculating the propagator from (2) using the observed data (Penland 1996):

$$\mathbf{L}^{ST} = \hat{\tau}^{-1} \log[\mathbf{G}^{ST}(\hat{\tau})] = \hat{\tau}^{-1} \log[\mathbf{C}(\hat{\tau})\mathbf{C}^{-1}(0)], \quad (3)$$

where $\mathbf{C}(0)$ is the 0-lag covariance matrix and $\mathbf{C}(\hat{\tau})$ is the lagged covariance matrix of the system state vector $\mathbf{x}$ at a specified lag $\hat{\tau}$. We use a lag $\hat{\tau} = 3$ months for the LIM. Once $\mathbf{L}^{ST}$ is calculated, the propagator matrix for any lag τ is then calculated as $\mathbf{G}^{ST}(\tau) = \exp(\mathbf{L}^{ST}\tau)$.

In the CSLIM the seasonally varying dynamical system matrices $\mathbf{L}_i^{CS}$ are calculated separately for each month. Twelve covariance and $\hat{\tau} = 1$ month lagged covariance matrices are calculated, and then each monthly propagator is determined from

$$\mathbf{G}_i^{CS} = \mathbf{C}_i(\hat{\tau} = 1)\mathbf{C}_i^{-1}(0), \quad (4)$$

where i is the calendar month. Prior to using (4) a 3-month centered running mean is applied to the covariance and lagged covariance matrices to counter the sampling error introduced by the 12-fold increase in calculated parameters (see Shin et al. 2021). In the CSLIM the seasonally varying dynamical system matrices $\mathbf{L}_i^{CS}$ are then calculated separately for each month using (3). The full propagator over time τ is calculated via

$$\mathbf{G}_i^{CS}(\tau) = \mathbf{G}_{i+\tau-1}^{CS} \cdots \mathbf{G}_1^{CS} \mathbf{G}_{12}^{CS} \cdots \mathbf{G}_i^{CS}, \quad (5)$$

where it is understood that the subscript on $\mathbf{G}^{CS}$ is modulo 12 (i.e., $\mathbf{G}_{12}^{CS}$ propagates December's state 1 month forward to January, and would be left multiplied by $\mathbf{G}_1^{CS}$ and so forth to continue propagation). Note that the propagator is a function of lag τ only in the LIM and both lag *and* initial month i in the CSLIM.

The state vector for this analysis consists of the nine leading principal components (PCs; 79% variance explained) of sea surface temperature (SST) from the HadISST dataset (Rayner et al. 2003) and five leading PCs (63% variance explained) of sea surface height (SSH) from the ECMWF Ocean Reanalysis System (ORAS4; Balmaseda et al. 2013) over the region 100°E–75°W, 25°S–25°N over the period 1958–2017. All data are detrended prior to computing the PCs. The full state vector is compiled via scaling the PCs $\mathbf{z}$ as follows:

$$\mathbf{x} = \left[(\mathbf{z}_{SST,1-9})\Big/\sqrt{\sum_{all}\lambda_{SST}} \quad (\mathbf{z}_{SSH,1-5})\Big/\sqrt{\sum_{all}\lambda_{SSH}}\right], \quad (6)$$

where $\mathbf{z}$ is the PC of the associated field and λ is the associated eigenvalue (hence, each field is scaled by the square root of its total variance).

b. Growth calculations

This study focuses on how initial structures grow into "canonical" ENSO events, and ENSO events with CP or EP
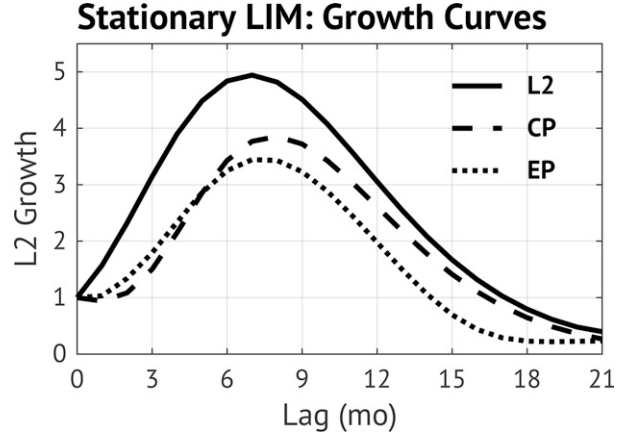

FIG. 1. "Maximum amplitude" curve showing growth of optimal initial conditions from the stationary LIM. Curves denote growth from the L2 (solid line), CP (dashed line), and EP (dotted line) optimal initial conditions. Although optimal initial conditions are calculated under different final norms, all growth is evaluated under an L2 norm to allow comparison (see the text).

SST characteristics. Growth of an initial structure via the deterministic dynamics [the homogeneous part of (1)] over a time period τ is calculated as

$$\mu_{M,N}(\tau) = \frac{\|\mathbf{x}(\tau)\|_N^2}{\|\mathbf{x}(0)\|_M^2} = \frac{\mathbf{x}^T(\tau)\mathbf{N}\mathbf{x}(\tau)}{\mathbf{x}^T(0)\mathbf{M}\mathbf{x}(0)} = \frac{\mathbf{x}^T(0)\mathbf{G}^T(\tau)\mathbf{N}\mathbf{G}(\tau)\mathbf{x}(0)}{\mathbf{x}^T(0)\mathbf{M}\mathbf{x}(0)}, \quad (7)$$

where M and N refer to initial and final norms, respectively; $\mathbf{M}$ and $\mathbf{N}$ are defined below. Initial optimal patterns $\mathbf{p}$ that maximize growth over a time period τ are identified via solving the generalized eigenvalue problem (Zanna and Tziperman 2005; Martinez-Villalobos and Vimont 2016):

$$\mathbf{G}_\tau^T\mathbf{N}\mathbf{G}_\tau\mathbf{p} = \mu_{M,N}(\tau)\mathbf{M}\mathbf{p}. \quad (8)$$

Eigensolutions $\mathbf{p}$ are initial conditions that optimally grow in the direction that defines the final norm $\mathbf{N}$, subject to potential constraints from the initial norm $\mathbf{M}$. These initial conditions evolve into patterns $\mathbf{r} = \mathbf{G}(\mu)\mathbf{p}$ over the time period τ. The leading eigenvector $\mathbf{p}$ and its evolved state τ months later will be referred to, respectively, as the "optimal" and "final" growth patterns. Note that for the CSLIM optimal patterns depend on both the lag τ *and* the initial month (even for $\tau = 12$ months), which differs from the LIM in which optimals are not seasonally dependent.

CP and EP norms are defined from this state vector via the same norm kernels as used in Vimont et al. (2014) to investigate initial structures that optimally grow toward CP or EP ENSO events:

$$\mathbf{n}_{CP} = \left[1/\sqrt{(2\lambda_1)}, \quad 1/\sqrt{(2\lambda_2)}, \quad 0, \quad 0, \quad \cdots\right] \quad \text{and}$$

$$\mathbf{n}_{EP} = \left[1/\sqrt{(2\lambda_1)}, \quad -1/\sqrt{(2\lambda_2)}, \quad 0, \quad 0, \quad \cdots\right].$$
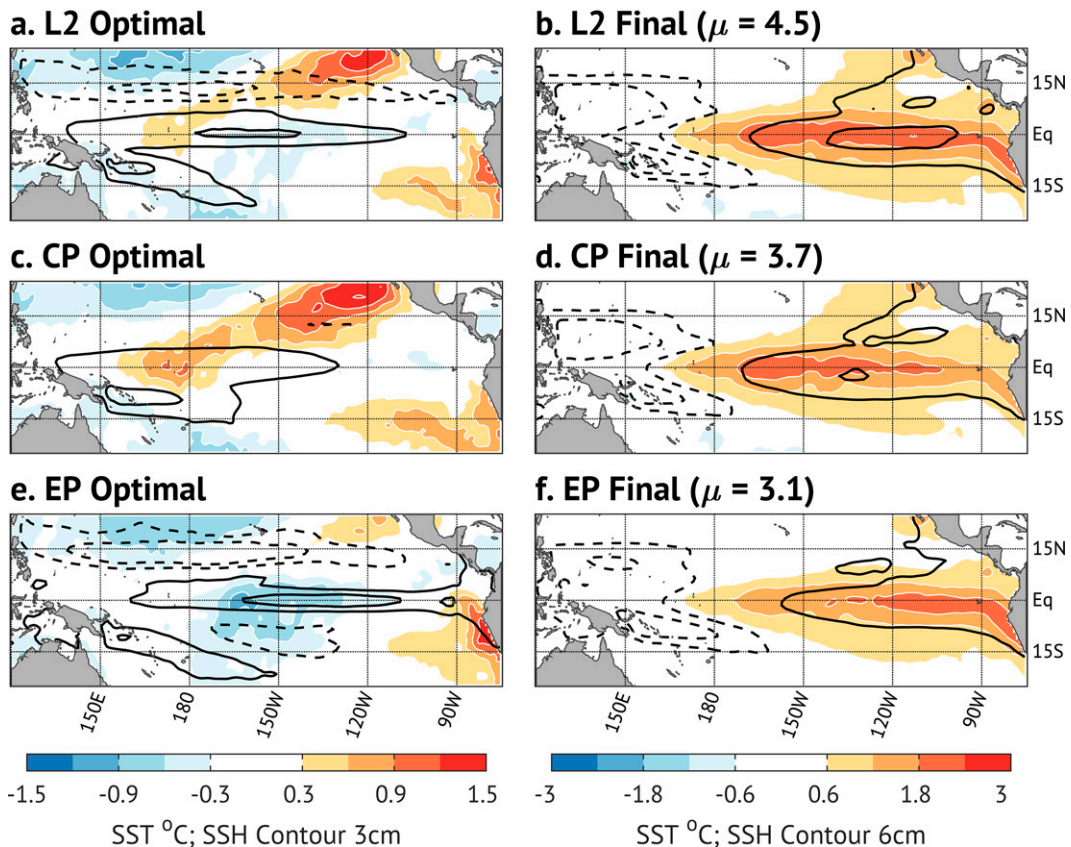
Stationary LIM 9mo Optimal Growth Structures

Fɪɢ. 2. Nine-month (left) optimal initial and (right) final structures calculated from the stationary LIM, under an (a),(b) L2; (c),(d) CP; and (e),(f) EP final norm. Total growth μ is listed for each final condition. SST is shaded, and SSH is contoured, with solid black contours indicating positive SSH anomalies, dashed black contours indicating negative SSH anomalies, and the zero contour omitted. Overall amplitude is arbitrary, but all features can be compared relative to each other.

These norm kernels are based on the findings of Takahashi et al. (2011), who show that CP and EP ENSO events can be well approximated as the sum or difference of the first two PCs of tropical Pacific SST, which are the first two elements of the state vector used here. The final norm matrix is calculated as $\mathbf{N} = \mathbf{n}^T\mathbf{n} + \varepsilon\mathbf{I}$, where $\varepsilon = 10^{-9}$ is added to the diagonal for numerical stability (Tziperman et al. 2008). We use an L2 norm for all initial norms (i.e., $\mathbf{M} = \mathbf{I}$, the identity matrix, for all analyses), and as a final norm when considering "canonical" ENSO events (in those cases, $\mathbf{N}_{L2} = \mathbf{I}$).

In this paper, we use the phrase "amplitude" to describe the squared norm of a vector [e.g., the numerator or denominator in (7)], and "growth" or "amplification" to describe the full result from (7) (i.e., a metric that depends on the initial *and* final amplitude). Both amplitude and growth, though, are norm dependent, and hence a common norm is needed to compare growth from different optimals, such as the CP optimal and EP optimal (as each would maximize growth toward its respective norm). An obvious choice for comparing growth

is to calculate it within the L2 norm [i.e., $\mathbf{N} = \mathbf{I}$ in (7)] as this describes the growth of domain-integrated variance within the state space of the model (6). *For all analysis herein, different final norms are only used to define optimal initial structures from (8), and amplitude or growth is always calculated using the L2 final norm [e.g., (7)].*

3. Optimal growth for the LIM and CSLIM

a. Section summary

How does seasonality affect growth of "canonical," CP, and EP ENSO events? Analysis of the LIM (Figs. 1 and 2) and CSLIM (Figs. 3–5) shows that seasonality strongly influences the growth and evolution of ENSO events with CP and EP characteristics. The stationary LIM appears to blend and obscure these important seasonal differences. The CSLIM shows that all types of ENSO events experience maximum growth toward final states at the end of the calendar year (Fig. 3), originating from boreal spring initial states that include a deepened thermocline across the equatorial
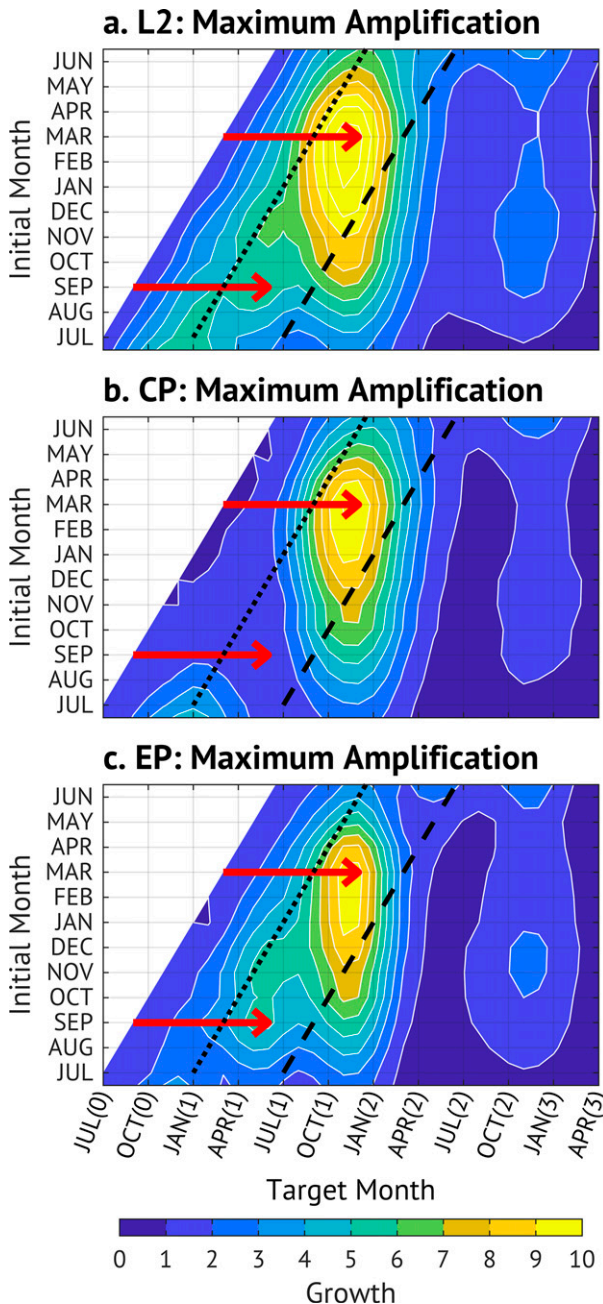
FIG. 3. Seasonal "maximum amplitude" curves showing growth of optimal initial conditions calculated from the CSLIM under (a) L2, (b) CP, and (c) EP final norms. Each plot shows growth from a given month's initial optimal (*y* axis) through a given final (target) month (*x* axis). Red arrows indicate 9-month evolution from March to December, and from September to June; these time periods are used in Figs. 4, 5, and 9–12. For reference, diagonal lines indicate 6- (dotted black line) and 12-month (dashed black line) lead times. Although optimal initial conditions are calculated under different final norms, all growth is evaluated under an L2 norm to allow comparison.

Pacific and off-equatorial SST anomalies in the eastern subtropics of both hemispheres (Fig. 4). The growth from March–December is consistent with the "delayed/recharge oscillator" theory of ENSO growth (Zebiak and Cane 1987; Schopf and Suarez 1988; Battisti 1988; Jin et al. 2008), with possible influence from subtropical SST anomalies that are consistent with the SFM. EP-type and "canonical" ENSO events also experience growth from September–June (Fig. 5), originating from deepened thermocline anomalies and *cold* equatorial SST in the central equatorial Pacific. In contrast, CP-type events evolve from September–June via structures that resemble the North Pacific meridional mode (NPMM), suggesting a more important role for the SFM throughout boreal winter and spring.

b. Analysis of growth

Maximum growth of ENSO structures via (7) is evaluated as a function of lag for the LIM and plotted as a "maximum amplification" (MA) curve in Fig. 1. Again, for each curve, optimal initial conditions are calculated under a particular prescribed norm, but growth is calculated under an L2 norm so that curves represent a common metric of domain-integrated variance. By construction, the growth of domain-integrated variance under the L2 norm is maximized for an optimal initial condition calculated under the same norm (the solid black curve in Fig. 1) and peaks at around 7-month lead time. Growth is smaller for initial conditions calculated under the CP and EP norms and peaks at around 8 and 7 months, respectively.

For the stationary LIM, the $\tau = 9$ months L2, CP, and EP optimal and final growth patterns are shown in Fig. 2, and, like the MA curves, largely resemble results in Vimont et al. (2014). The final conditions under an L2-norm indicate growth into a mature ENSO event, and growth under the CP and EP norms show similar final ENSO structures but with CP and EP characteristics. The CP optimal resembles the PMM (Chiang and Vimont 2004), and the EP optimal exhibits a zonal dipolar structure in SST and a deepened thermocline (inferred from SSH) along the equator. All optimals exhibit warm SST anomalies in the southeastern tropical Pacific (around 15°S), but the L2 and EP optimals do not show SST anomalies extending across the Pacific around 25°S, in contrast to findings in Vimont et al. (2014).

Unlike the stationary LIM, growth in the CSLIM depends on both lag and seasonal timing, so a different MA curve is calculated for each initial month. These MA curves are shown in Fig. 3 and reveal a fundamentally different behavior than that calculated by the LIM. For all norms, the maximum growth is achieved for late boreal winter initial conditions that evolve through the end of the calendar year (top red arrows in Fig. 3). A major difference between the growth of CP, and EP or canonical initial conditions, is seen for 6–9-month lead times with target final conditions in late boreal spring (bottom red arrows in Fig. 3). There, CP initial conditions experience much less growth than EP or canonical initial conditions. These differences will be explored further below.

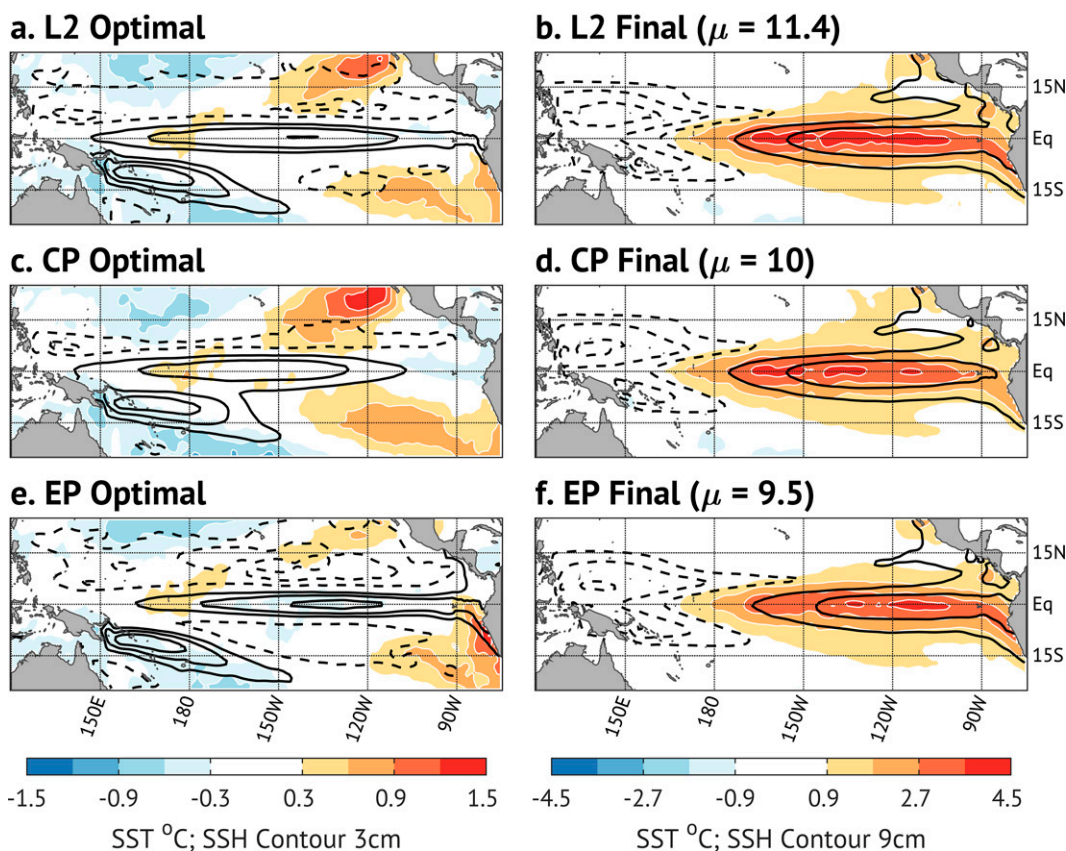# CSLIM 9mo (MAR to DEC) Optimal Growth Structures

FIG. 4. Nine-month, March–December (left) optimal initial and (right) final structures calculated from the CSLIM, under an (a),(b) L2; (c),(d) CP; and (e),(f) EP final norm. Total growth μ is listed for each final condition. SST is shaded, and SSH is contoured, with solid black contours indicating positive SSH anomalies, dashed black contours indicating negative SSH anomalies, and the zero contour omitted. Overall amplitude is arbitrary, but all features can be compared relative to each other.

The optimal initial and final growth patterns in the CSLIM depend on both lag and initial month and are shown for $\tau = 9$ months for March initial conditions (March–December) in Fig. 4 and for September initial conditions (September–June) in Fig. 5. In contrast to results from the stationary LIM, the March–December optimal initial and final conditions for all norms (Fig. 4) are more alike than different. The L2, CP, and EP optimals all include PMM-like initial SST anomalies (albeit more pronounced for the CP optimal), deepened thermocline anomalies along the equator (albeit more pronounced and shifted eastward for the EP optimals), and warm SST anomalies in the southeastern equatorial Pacific (near around 15°S, 90°–120°E). The final states for the optimal CP and EP initial conditions also exhibit more similarities than differences, with much less distinction between CP and EP final SST structures than observed from the LIM. Still, the final states do include subtly different centers of maximum SST anomalies, in line with their respective norms.

Based on the MA curves in Fig. 3, it is not surprising that the March–December structures exhibit very little difference

for L2, CP, and EP norms. In contrast, the September–June CP optimal initial and final conditions for the CSLIM (Figs. 5c,d) have very different structures than those calculated under the L2 or EP norms (in Figs. 5a,b and 5e,f, respectively; the L2 and EP optimal initial and final conditions are nearly identical). The most obvious difference between the CP, and EP or L2 optimals, is the strong PMM-like SST anomalies in the CP optimal (Fig. 5c) that is not present in the other initial state. This evolves, albeit with almost no growth, into a clear CP-type ENSO event by the following June. Both the EP and L2 initial states evolve into an ENSO event that is concentrated in the eastern equatorial Pacific.
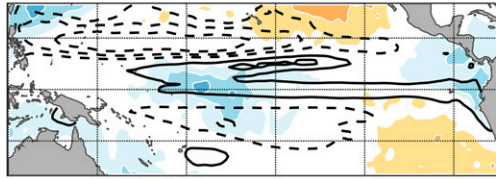
4. The "ENSO mode," and its relationship to modal and nonnormal growth
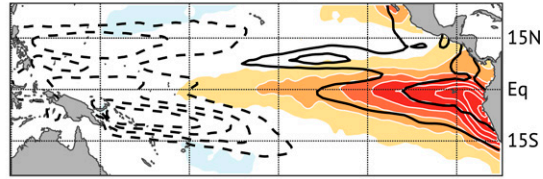
a. Section summary

This section identifies a seasonally varying "ENSO mode" and investigates its role in producing the growth of CP and

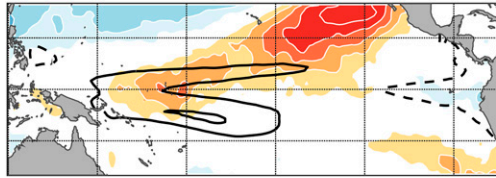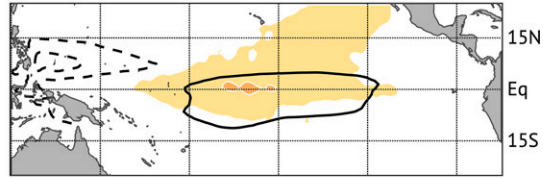## CSLIM 9mo (SEP to JUN) Optimal Growth Structures
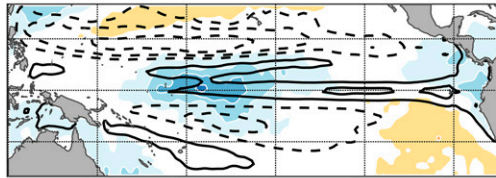

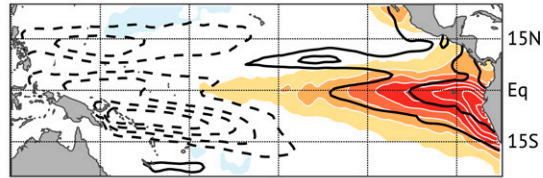### a. L2 Optimal

b. L2 Final ($\mu = 5.8$)

c. CP Optimal

d. CP Final ($\mu = 1.3$)

e. EP Optimal

f. EP Final ($\mu = 5.3$)

-1.5   -0.9   -0.3   0.3   0.9   1.5

SST °C; SSH Contour 3cm

-3   -1.8   -0.6   0.6   1.8   3

SST °C; SSH Contour 6cm

FIG. 5. As in Fig. 4, but showing the 9-month, September–June (left) optimal initial and (right) final structures calculated from the CSLIM. Note the different contour interval and range in color shading for final conditions as compared with Fig. 4.

EP ENSO structures. The ENSO mode evolves in a manner consistent with the delayed/recharge oscillator model, and experiences its maximum instantaneous modal growth rate from August–October. The modal growth rate is responsible for the timing of the late boreal autumn maximum in the growth of CP, EP, and canonical ENSO events, and explains the similar spatial structure of final structures that occur toward the end of the calendar year. However, the nonnormal "masking" of initial conditions is necessary for realizing the full growth of ENSO structures through the late calendar year. Nonnormal masking of initial conditions is also responsible for the growth of EP structures from boreal autumn through late spring, as the ENSO mode decays over that time period. In contrast, the evolution of CP events from boreal autumn through late spring is not strongly influenced by the ENSO mode. During this time, CP structures appear to evolve via dynamics associated with tropical meridional modes. Hence, EP events occur as the ENSO mode's slow seasonal evolution allows it to "emerge" while more rapid Floquet modes evolve and decay. CP events occur when initial conditions have a large contribution from meridional mode-like structures.

b. ENSO mode structure

Previous research (Penland and Sardeshmukh 1995; Thompson and Battisti 2000; Newman et al. 2011a; Shin et al. 2021), combined with the similarity of the $\tau = 9$ month March–December L2, CP, and EP optimal initial and final growth structures in the CSLIM, suggest the importance of an "ENSO mode" that plays a role in the growth of ENSO-like structures. In the CSLIM framework, solutions to the homogeneous equation in (1) are obtained via "Floquet theory" and have the following form:

$$\mathbf{x} = \mathbf{q}_k \exp(\mu_k t), \tag{9}$$

where $\mathbf{q}_k$ is the kth cyclic eigenvector with a 12-month period and μ_k is the complex Floquet exponent (Thompson and Battisti 2000; Johnson et al. 2000b; Shin et al. 2021). As described in von Storch et al. (1995) and Shin et al. (2021), eigenanalysis of each of the 12-month propagators (5) yields the seasonally varying Floquet modes (left eigenvectors), their associated adjoints (right eigenvectors), and Floquet exponents (which do not vary seasonally). The Floquet exponents are shown in Fig. 6 together with the eigenspectrum of
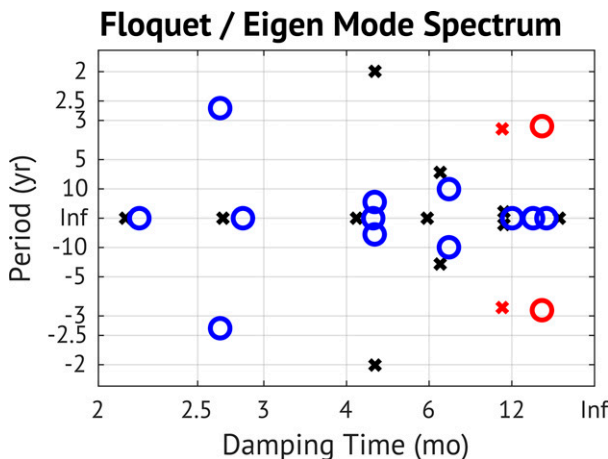
Floquet / Eigen Mode Spectrum

FIG. 6. Floquet exponents (open circles) from the CSLIM and eigenspectrum (times signs) from the stationary LIM, expressed as a period (yr) and damping time scale (months). The red open circles and times signs indicate the "ENSO mode."

the stationary LIM. Both the Floquet exponents and LIM eigenspectrum include a conjugate pair of oscillatory modes (highlighted in red in Fig. 6) with interannual periods (38 months for the CSLIM and 39 months for the LIM) and long damping time scales (19 months for the CSLIM and 11 months for the LIM).

The spatial structures of the Floquet mode 1 (Floquet mode 2 is its complex conjugate) for December and June are shown in Fig. 7. The real component bears a strong resemblance to the seasonal structure of a mature ENSO event, and analysis of other months confirms a similar structure (see Smith et al. 2014). The imaginary component is orthogonal to the real component by construction, and evolves into the real

component over one-quarter of the oscillation time scale. The imaginary component of Floquet mode 1 includes positive SST and deepened thermocline anomalies along the equator that are flanked by cool SST anomalies and shoaled thermocline anomalies around $10°~15°$ on either side of the equator. The evolving spatial structure resembles the delayed/recharge oscillator model with deepened equatorial thermocline anomalies across the entire Pacific that evolve eastward into a surface ENSO event (Battisti 1988; Jin et al. 2008); a similar ENSO-mode eigenvector is found by Xie and Jin (2018) in analysis of CP and EP structures in the Zebiak and Cane (1987) model. Based on the similarity between the time scale and spatial structures of Floquet modes 1 and 2 and known ENSO characteristics, and their similarity to the corresponding eigenmode in the stationary LIM (not shown but see Newman et al. 2011a) we refer to modes 1 and 2 as the "ENSO mode."

c. Modal and nonnormal growth

Growth of ENSO-like structures can occur via the seasonal and oscillatory evolution of the ENSO mode (modal growth) or interference with other nonorthogonal modes (nonnormal growth, described below). Modal growth can occur even if the mode is damped, as it must be for stationarity, and is due to the seasonal and oscillatory evolution of the complex Floquet mode. Growth through time occurs as the mode evolves from through its complex phase space (e.g., Penland and Sardeshmukh 1995) and is countered by damping via the Floquet exponents (9). Additionally, unlike eigenvectors from the stationary LIM, the Floquet modes can also experience modal growth as they evolve throughout the seasonal cycle (von Storch et al. 1995). The maximum (L2) modal growth of the ENSO mode, plotted in Fig. 8a, shows a seasonality consistent with that seen in Fig. 3: the maximum growth occurs for late-calendar-year final states (October and November, which is
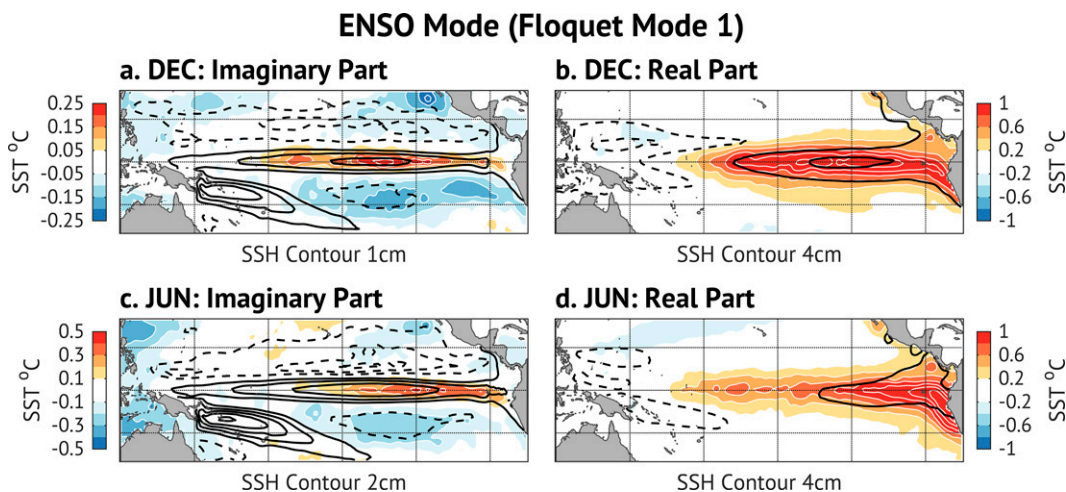
ENSO Mode (Floquet Mode 1)

FIG. 7. Spatial structure of the ENSO mode during (a),(b) December and (c),(d) June (monthly components of the leading Floquet mode from the CSLIM). Shown are the (left) imaginary and (right) real components. SST is shaded, and SSH is contoured, with solid black contours indicating positive SSH anomalies, dashed black contours indicating negative SSH anomalies, and the zero contour omitted. Overall amplitude is arbitrary, but all features can be compared relative to each other; note the difference in scale for (c).
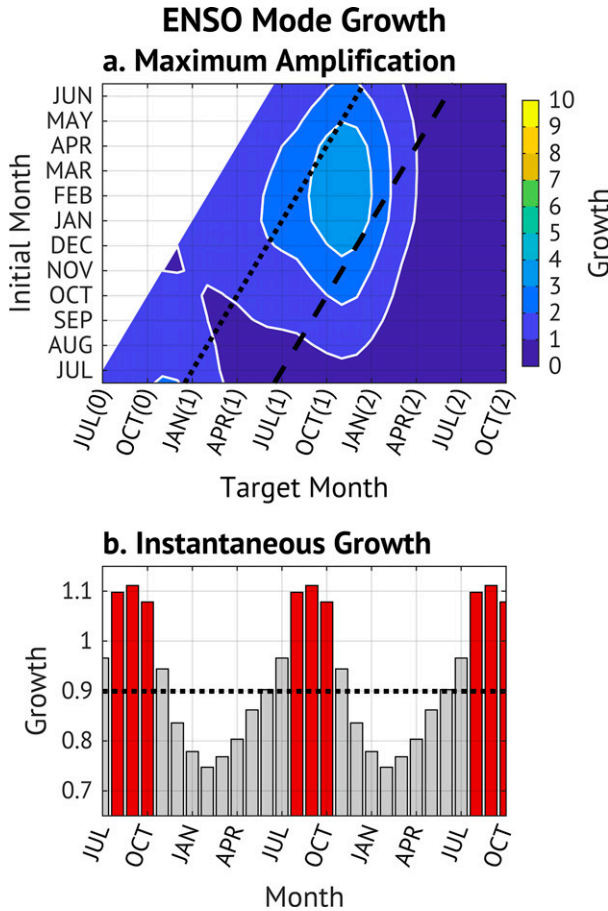
ENSO Mode Growth

a. Maximum Amplification

b. Instantaneous Growth

FIG. 8. Seasonal growth for the ENSO mode: (a) Maximum amplification, plotted as growth from a given initial month (y axis) through a given final (target) month (x axis). For reference, diagonal lines indicate 6- (dotted black line) and 12-month (dashed black line) lead times. (b) Monthly varying instantaneous growth rates of the seasonally varying ENSO mode (see the text), as well as the overall growth rate of the Floquet mode (horizontal dashed line).

about 1 month earlier than the full optimals) and is greatest when starting from initial conditions in boreal winter and spring (December–May). The maximum growth *rate* [Fig. 8b; calculated by propagating each month's unit-length complex ENSO mode structure forward one month and determining the amplitude: $r_k = \|\mathbf{G}_k^{CS}(1)q_k\|_{L2}^2$] occurs in September, with unstable growth rates ($r_k > 1$) occurring from August–October (see also Shin et al. 2021). A comparison of Figs. 8a and 8b shows that the ENSO mode's seasonally varying instantaneous growth rate (Fig. 8b) is responsible for the late-calendar-year timing of the maximum growth (Fig. 8a), and its subsequent rapid decay during the boreal winter and spring.

Despite its similar temporal evolution, the maximum modal amplification in Fig. 8 is much weaker than the maximum growth seen in Fig. 3, highlighting a role for nonnormal modal interference for optimal growth in Fig. 3. The CSLIM is nonnormal, and as a result, the Floquet modes are nonorthogonal. Thus, the optimal initial conditions in Figs. 4 and 5

include contributions from the ENSO mode as well as destructive interference from additional Floquet modes that interfere with, or in this case mask the ENSO mode's initial contribution (Farrell and Ioannou 1996; Newman et al. 2011a; Henderson et al. 2020; Shin et al. 2021). One can focus on the contribution from the ENSO mode (or remaining modes) via reconstructing the optimal initial conditions (from section 3) to retain only the ENSO mode (or all modes except the ENSO mode):

$$\mathbf{p}_{k,\text{ENSO}} = \sum_i \mathbf{q}_{k,i}\left(\mathbf{a}_{k,i}^{T}\mathbf{p}_k\right), \qquad (10)$$

where $\mathbf{a}_{k,i}^{T}$ is the nonconjugate transpose of the ith adjoint Floquet mode for month k, $\mathbf{p}_k$ is the original optimal [the eigensolution to (8)] for a given initial month, and the sum over i is taken for modes 1–2 (the ENSO mode) or the remaining modes 3–14 (all modes except the ENSO mode). The reconstructed optimal $\mathbf{p}_{k,\text{ENSO}}$ is propagated forward over a time interval $t = \tau$, resulting in $\mathbf{r}_{\text{ENSO}} = \mathbf{G}^{CS}(\tau)\mathbf{p}_{k,\text{ENSO}}$. Recall that, despite nonorthogonality, the Floquet modes evolve independently so the final state is still solely within the space of the ENSO mode.

The ENSO mode's role in producing growth through modal evolution and nonnormal interference for CP and EP events is clearly seen by propagating the full and reconstructed optimal initial conditions forward through the 9-month period over which they are defined. Figures 9–12 show the temporal evolution from 9-month optimal initial conditions, including the evolution from the full optimal (left column), the contribution from the ENSO-mode [middle column; reconstructed as in (10)] and the contribution from the non-ENSO modes [right column; reconstructed as in (10) except summed over all modes *except* the ENSO mode]. Recall that individual Floquet modes are solutions to the homogeneous equation in (1) and thus the middle and right columns of Figs. 9–12 sum to equal the left column [although because they are not orthogonal, their L2 amplitude (domain-integrated variance) does not sum to equal the full amplitude].

The ENSO mode's contribution to the growth of the March 9-month optimals is evident in the evolution of the CP and EP optimals in Figs. 9 and 10, respectively. In both cases, the ENSO mode contributes similar structures to the optimal initial conditions (top row) and grows as it evolves through the following 9 months. Despite the different initial ENSO mode *amplitudes* γ for the CP and EP initial condition (top row of Figs. 9 and 10), the 9-month ENSO mode *growth* (the ratio of final to initial ENSO mode amplitude of 3.35 for the CP and 3.67 for the EP cases) and initial spatial structures (i.e., initial phases) are comparable, indicating that the ENSO mode plays a similar role in the evolution of both structures at this time of year.

The remaining modes contribute in two different ways to the CP and EP evolution over the 9-month evolution: by (i) amplifying growth via masking the ENSO mode in the initial condition [the denominator in (5)], or (ii) affecting the structure of the resulting final condition through their evolution. For both CP and EP optimals, the remaining

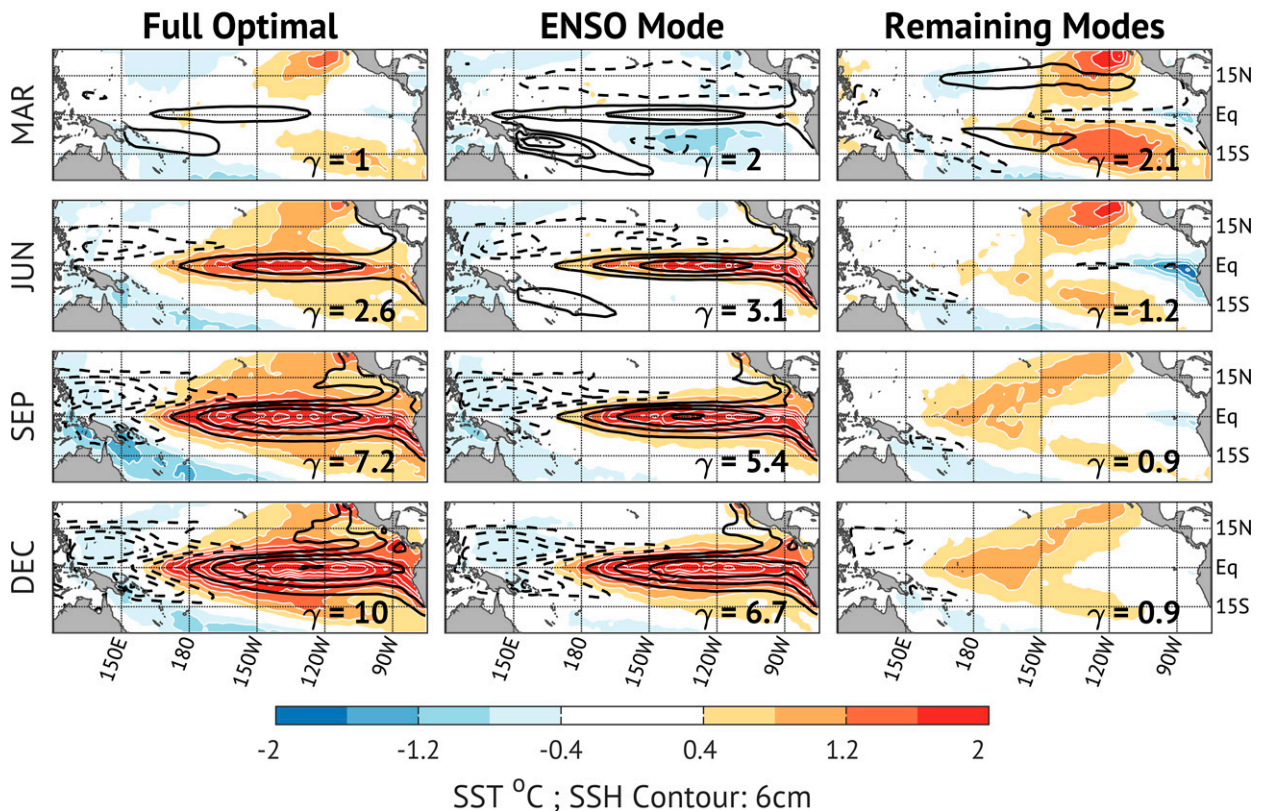# CSLIM 9mo (MAR to DEC) CP Optimal Evolution

FIG. 9. Spatiotemporal evolution of the March, 9-month CP optimal initial condition. Shown is the evolution of the (left) full optimal, (center) ENSO mode contribution, and (right) contribution from all modes *except* the ENSO mode. The amplitude γ (domain integrated variance) of each map is shown. SST is shaded, and SSH is contoured, with solid black contours indicating positive SSH anomalies, dashed black contours indicating negative SSH anomalies, and the zero contour omitted. Overall amplitude is arbitrary, but all features can be compared relative to each other.

modes contribute to rapid growth via (i) masking the initial conditions: indeed, the *growth* of the full optimal (10 for the CP optimal and 9.5 for the EP optimal) is more than 2.5 times the growth of the ENSO mode on its own (recall that γ represents amplitude, or domain-integrated variance in Figs. 9 and 12). For the CP events, the additional modes also (ii) contribute to the continued evolution via structures that continue to evolve westward and equatorward to help generate SST anomalies in the central equatorial Pacific (between 165°E and 150°W) through the following December (Fig. 9, right column). This equatorward and westward propagation of hemispherically symmetric structures is similar to the theoretical analysis of meridional mode evolution (Martinez-Villalobos and Vimont 2017), and may also result from zonal advection as found by Xie and Jin (2018) in the Zebiak and Cane (1987) model.

The 9-month evolution from the September CP optimal (Fig. 11) shows very little contribution from the ENSO mode (middle column). Indeed, the PMM-like initial SST state for the full optimal (Fig. 11, top left) is captured as the ENSO mode *offsets* the amplitude of non-ENSO mode anomalies in

the eastern and southeastern equatorial Pacific. The remaining modes evolve equatorward and westward, growing to produce CP SST anomalies by December before decaying through the following June. The final state includes similar amplitude contributions from both the ENSO mode and remaining modes; however, it is clear that the non-ENSO modes are important for generating the CP structure throughout the CP evolution.

For the September EP optimal, the non-ENSO modes largely offset the ENSO mode in the initial conditions (Fig. 12, top row), similar to the role they play for the March optimal. However, in this case the ENSO mode only undergoes a short period of modal growth through December and then slowly decays through June. The overall growth of the EP event, with an equatorial SST anomaly centered far to the east, results from the non-ENSO modes decaying so rapidly (Fig. 12, right column) that they allow the weakening ENSO mode amplitude to emerge. The difference in initial ENSO mode amplitude between the September and March EP initial conditions also points to a seasonality in the effectiveness of the non-ENSO modes in masking the the ENSO mode.

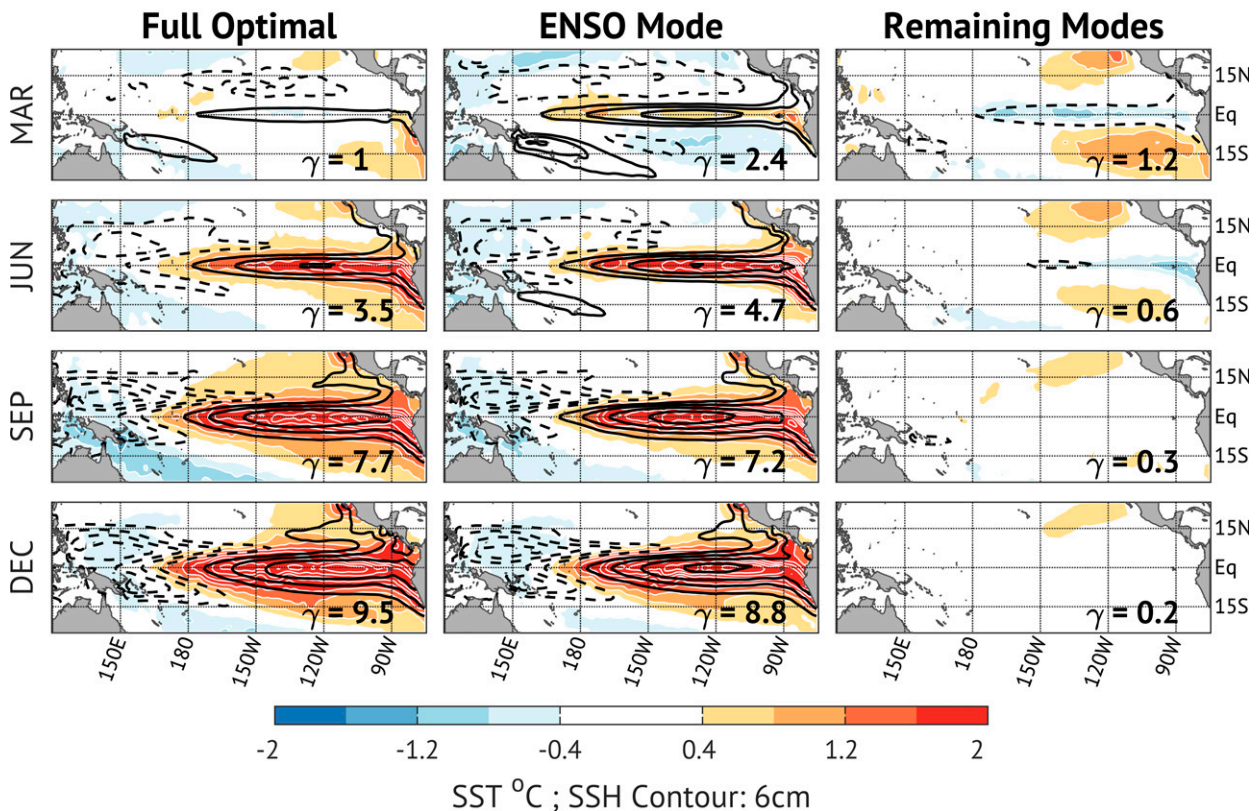## CSLIM 9mo (MAR to DEC) EP Optimal Evolution

FIG. 10. As in Fig. 9, but for the March 9-month EP optimal.

During September, these additional modes are more effective at producing nonnormal growth as they more effectively cover up the ENSO mode.

5. Summary and discussion

a. Summary

A cyclostationary linear inverse model was used to investigate the seasonally varying spatiotemporal growth of ENSO events with SST structures ranging between canonical (L2 growth), CP, and EP states. Analysis shows that the evolution of all types of ENSO events exhibits strong seasonality, with growth maximizing for final conditions near the end of the calendar year (around November–December). This seasonality is also found in a pair of Floquet modes (the ENSO mode) that experience maximum instantaneous growth rate from August–October, leading to maximum total growth in late boreal autumn (October–November). The analysis also shows weak growth toward either L2 or EP final conditions from boreal autumn through early boreal summer (September–June), but significant growth over that time does not occur for CP structures. The seasonality of ENSO growth is not consistent with findings that the coupling strength is strongest during boreal spring due to seasonality of low-level atmospheric convergence (Philander 1983; Tziperman et al. 1997). Tziperman et al. (1997)

do show that other factors such as SST gradients and upwelling also contribute to ENSO seasonality in the Zebiak and Cane (1987) model. Initial analysis of the dynamical system matrix here (not shown) suggests that thermocline/SST feedbacks may also play an important role in seasonality of ENSO growth.

Within the nonnormal, seasonally varying system, there are multiple ways in which a particular initial condition can grow and evolve over a given time. First, independent modal growth can occur as a single Floquet mode pair (the ENSO mode) evolves through its phase trajectory. This seasonality is critical for the boreal late autumn maximum amplification for all types of events since the instantaneous growth rate of the ENSO mode peaks from August–October. While the ENSO mode is critical for the development of boreal late autumn ENSO events, on its own, it is insufficient to explain the full growth of L2, CP or EP events. A second source of growth in the nonnormal system occurs due to rapidly decaying, nonorthogonal (but independently evolving) Floquet modes that "mask" the ENSO mode in the initial condition. This masking effect is the dominant cause of the growth of EP ENSO structures at all times of the year, demonstrating that the growth of EP events primarily results the emergence of the ENSO mode as additional modes die off.

A third mechanism for growth and evolution involves interference between Floquet modes to produce structures that do
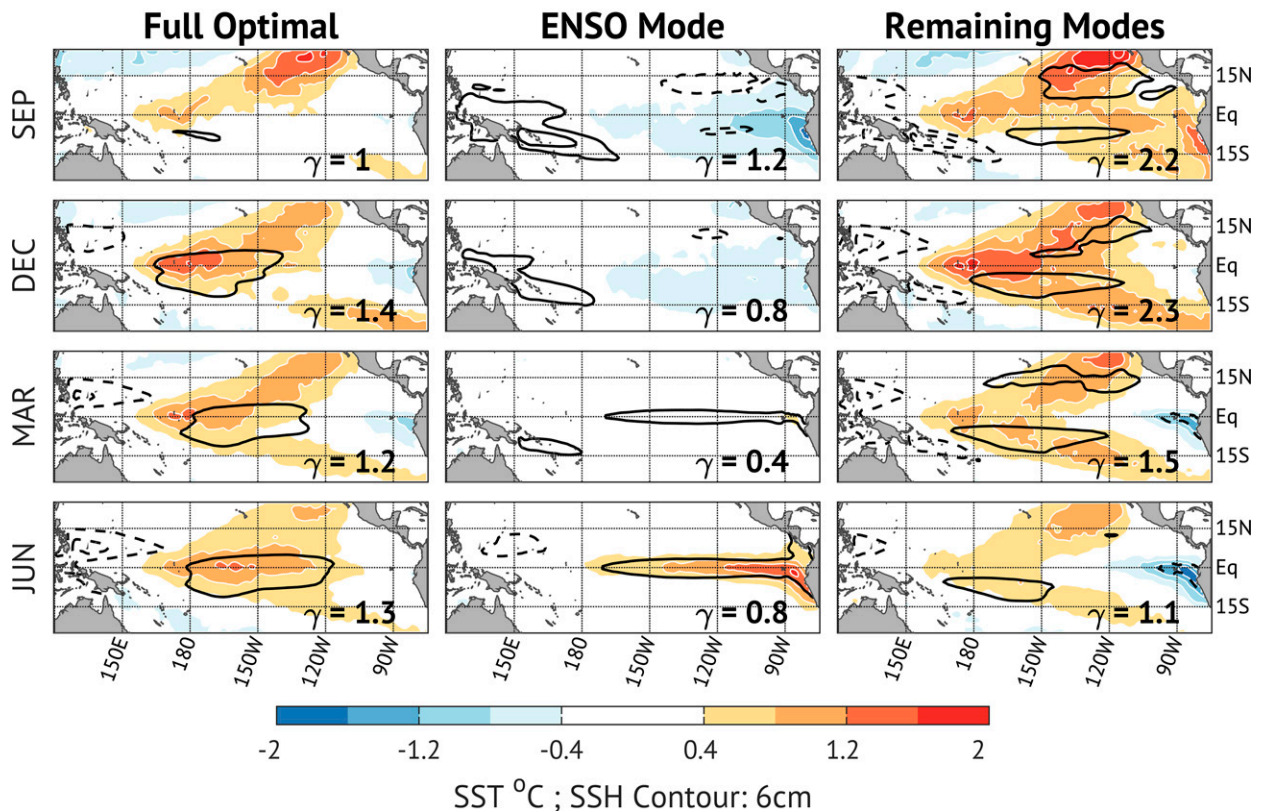
CSLIM 9mo (SEP to JUN) CP Optimal Evolution

FIG. 11. As in Fig. 9, but for the September 9-month CP optimal.

not exist solely within a single mode. In this case, the superposition of the Floquet modes does not simply mask the initial conditions but is also important for the full evolution of a particular event's structure. This mechanism occurs to some extent for both EP and CP events, but is much more prevalent in the evolution of CP-type ENSO events. The non-ENSO modes contribute a hemispherically symmetric structure that evolves westward and equatorward for these CP-type events, amplifying SST anomalies in the central equatorial Pacific and driving the ENSO event toward a CP-type structure. The importance of these non-ENSO modes suggests that physical processes outside of the delayed/recharge oscillator paradigm are responsible for generating CP events. For example, the off-equatorial SST structures strongly resemble theoretical models of meridional mode evolution (Martinez-Villalobos and Vimont 2017) though additional analysis is needed to confirm that those dynamics are present. This mechanism appears to be the dominant growth mechanism for short (3–4 months) growth of CP events, even during boreal autumn when the ENSO mode is temporarily unstable.

b. Discussion

What does this analysis tell us about the nature of ENSO events, including events with CP or EP characteristics? First, there is a strong seasonality to the deterministic growth and evolution of ENSO events that is influenced by the seasonality of the ENSO mode itself. The ENSO mode's seasonal growth during August–October causes that mode to dominate the deterministic evolution of all types of events through boreal autumn. The dominance of the ENSO mode growth during boreal autumn suggests that long-range deterministic ENSO predictions are not likely to be able to distinguish between CP or EP ENSO characteristics through late boreal autumn. Additionally, ENSO events do not tend to grow (along a deterministic trajectory) toward CP-type structures in late boreal spring. This lack of growth is due to the seasonally varying *structure* of the ENSO mode, which in late boreal spring has strong EP characteristics. Thus, the seasonal variation in growth and structure of the ENSO mode plays an important role in the timing of ENSO variability, its seasonally varying spatial structure, and its predictability.

Second, separating event evolution into contributions from the ENSO mode and remaining modes provides insight into the events' dynamics. ENSO events with EP characteristics occur as the ENSO mode's slow seasonal evolution allows it to emerge while additional Floquet modes rapidly evolve and decay. These EP events are largely driven by dynamics that are consistent with the delayed/recharge oscillator theories of ENSO variability, with deepened thermocline anomalies
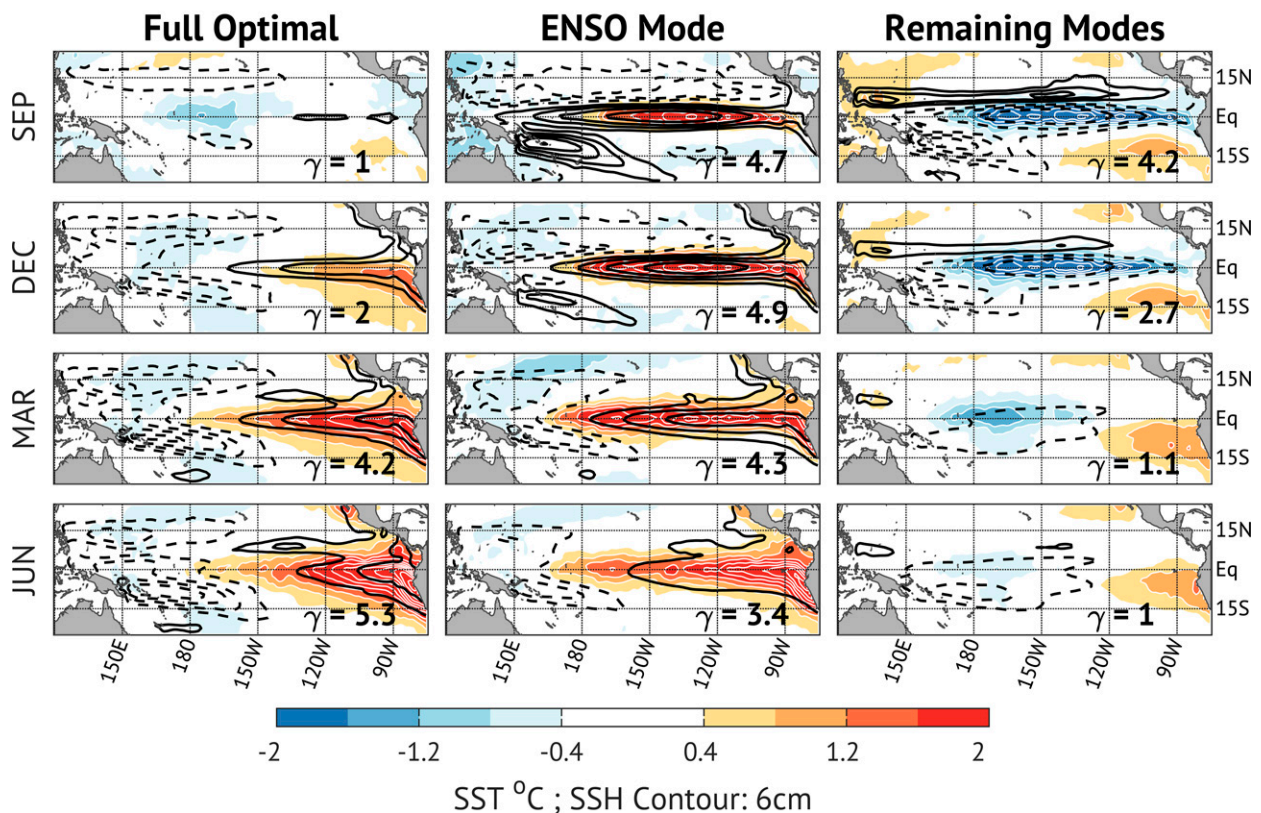
FIG. 12. As in Fig. 9, but for the September 9-month EP optimal.

along the equator evolving into warm SST anomalies in the eastern Pacific several months later (see Figs. 10 and 12). Events with CP structures occur as additional Floquet modes with meridional mode-like structures contribute to the spatial structure of the evolving event. These CP events are more strongly associated with off-equatorial modes that evolve westward, producing SST anomalies in the central equatorial Pacific by processes that do not appear to include strong thermocline anomalies (e.g., WES-feeedbacks, or zonal advection). The decomposition of event evolution into these separate Floquet modes may be useful in diagnosing individual events' evolution and predictability, and in identifying the source of biases in climate model representation of ENSO variability.

Note that any individual ENSO event will involve some combination of all of these mechanisms, leading to a rich set of ENSO structures that may be observed for any given event. Further, the full seasonal evolution of CP or EP final states will also depend on how seasonally varying structures of stochastic forcing excite particular combinations of Floquet modes and their resulting growth structures. The analysis herein provides an initial look at the deterministic evolution of seasonally varying growth structures. Additional analysis is needed to explore how these mechanisms, together with

contributions from nondeterministic stochastic forcing, combine to contribute to individual events' evolution and prediction.

REFERENCES

Alexander, M. A., D. J. Vimont, P. Chang, and J. D. Scott, 2010: The impact of extratropical atmospheric variability on ENSO: Testing the seasonal footprinting mechanism using coupled model experiments. *J. Climate*, **23**, 2885–2901, https://doi.org/10.1175/2010JCLI3205.1.

Ashok, K., S. K. Behera, S. A. Rao, H. Weng, and T. Yamagata, 2007: El Niño Modoki and its possible teleconnection. *J. Geophys. Res.*, **112**, C11007, https://doi.org/10.1029/2006JC003798.

Balmaseda, M. A., M. K. Davey, and D. L. Anderson, 1995: Decadal and seasonal dependence of ENSO prediction skill. *J. Climate*, **8**, 2705–2715, https://doi.org/10.1175/1520-0442(1995)008<2705:DASDOE>2.0.CO;2.

——, K. Mogensen, and A. T. Weaver, 2013: Evaluation of the ECMWF ocean reanalysis system ORAS4. *Quart. J. Roy. Meteor. Soc.*, **139**, 1132–1161, https://doi.org/10.1002/qj.2063.

Barnston, A. G., S. Li, S. J. Mason, D. G. Dewitt, L. Goddard, and X. Gong, 2010: Verification of the first 11 years of IRI's seasonal climate forecasts. *J. Appl. Meteor. Climatol.*, **49**, 493–520, https://doi.org/10.1175/2009JAMC2325.1.

Battisti, D. S., 1988: Dynamics and thermodynamics of a warming event in a coupled tropical atmosphere-ocean model. *J. Atmos. Sci.*, **45**, 2889–2919, https://doi.org/10.1175/1520-0469(1988)045<2889:DATOAW>2.0.CO;2.

——, D. J. Vimont, and B. P. Kirtman, 2019: 100 years of progress in understanding the dynamics of coupled atmosphere–ocean variability. *A Century of Progress in Atmospheric and Related Sciences, Meteor. Monogr.*, No. 59, Amer. Meteor. Soc., 8.1–8.57, https://doi.org/10.1175/AMSMONOGRAPHS-D-18-0025.1.

Capotondi, B. A., and Coauthors, 2015: Understanding ENSO diversity. *Bull. Amer. Meteor. Soc.*, **96**, 921–938, https://doi.org/10.1175/BAMS-D-13-00117.1.

Chen, X., and J. M. Wallace, 2015: ENSO-like variability: 1900–2013. *J. Climate*, **28**, 9623–9641, https://doi.org/10.1175/JCLI-D-15-0322.1.

Chiang, J., and D. Vimont, 2004: Analogous Pacific and Atlantic meridional modes of tropical atmosphere–ocean variability. *J. Climate*, **17**, 4143–4158, https://doi.org/10.1175/JCLI4953.1.

Farrell, B. F., and P. J. Ioannou, 1996: Generalized stability theory. Part I: Autonomous operators. *J. Atmos. Sci.*, **53**, 2025–2040, https://doi.org/10.1175/1520-0469(1996)053<2025:GSTPIA>2.0.CO;2.

Henderson, S. A., D. J. Vimont, and M. Newman, 2020: The critical role of non-normality in partitioning tropical and extratropical contributions to PNA growth. *J. Climate*, **33**, 6273–6295, https://doi.org/10.1175/JCLI-D-19-0555.1.

Hou, M., W. Duan, and X. Zhi, 2019: Season-dependent predictability barrier for two types of El Niño revealed by an approach to data analysis for predictability. *Climate Dyn.*, **53**, 5561–5581, https://doi.org/10.1007/s00382-019-04888-w.

Jin, E. K., and Coauthors, 2008: Current status of ENSO prediction skill in coupled ocean-atmosphere models. *Climate Dyn.*, **31**, 647–664, https://doi.org/10.1007/s00382-008-0397-3.

Jin, Y., Z. Liu, Z. Lu, and C. He, 2019: Seasonal cycle of background in the tropical Pacific as a cause of ENSO spring persistence barrier. *Geophys. Res. Lett.*, **46**, 13 371–13 378, https://doi.org/10.1029/2019GL085205.

Johnson, S., D. Battisti, and E. Sarachik, 2000a: Empirically derived Markov models and prediction of tropical Pacific sea surface temperature anomalies. *J. Climate*, **13**, 3–17, https://doi.org/10.1175/1520-0442(2000)013<0003:EDMMAP>2.0.CO;2.

——, ——, and ——, 2000b: Seasonality in an empirically derived Markov model of tropical Pacific sea surface temperature anomalies. *J. Climate*, **13**, 3327–3335, https://doi.org/10.1175/1520-0442(2000)013<3327:SIAEDM>2.0.CO;2.

Kao, H.-Y., and J.-Y. Yu, 2009: Contrasting eastern-Pacific and central-Pacific types of ENSO. *J. Climate*, **22**, 615–632, https://doi.org/10.1175/2008JCLI2309.1.

Kug, J.-S., F.-F. Jin, and S.-I. An, 2009: Two types of El Niño events: Cold tongue El Niño and warm pool El Niño. *J. Climate*, **22**, 1499–1515, https://doi.org/10.1175/2008JCLI2624.1.

Larkin, N. K., and D. E. Harrison, 2002: ENSO warm (El Niño) and cold (La Niña) event life cycles: Ocean surface anomaly patterns, their symmetries, asymmetries, and implications. *J. Climate*, **15**, 1118–1140, https://doi.org/10.1175/1520-0442(2002)015<1118:EWENOA>2.0.CO;2.

——, and ——, 2005: On the definition of El Niño and associated seasonal average U.S. weather anomalies. *Geophys. Res. Lett.*, **32**, L13705, https://doi.org/10.1029/2005GL022738.

Lenssen, N. J., L. Goddard, and S. Mason, 2020: Seasonal forecast skill of ENSO teleconnection maps. *Wea. Forecasting*, **35**, 2387–2406, https://doi.org/10.1175/WAF-D-19-0235.1.

Martinez-Villalobos, C., and D. J. Vimont, 2016: The role of the mean state in meridional mode structure and growth. *J. Climate*, **29**, 3907–3921, https://doi.org/10.1175/JCLI-D-15-0542.1.

——, and ——, 2017: An analytical framework for understanding tropical meridional modes. *J. Climate*, **30**, 3303–3323, https://doi.org/10.1175/JCLI-D-16-0450.1.

Neelin, J. D., D. S. Battisti, A. C. Hirst, F.-F. Jin, Y. Wakata, T. Yamagata, and S. E. Zebiak, 1998: ENSO theory. *J. Geophys. Res.*, **103**, 14 261–14 290, https://doi.org/10.1029/97JC03424.

Newman, M., and P. D. Sardeshmukh, 2017: Are we near the predictability limit of tropical Indo-Pacific sea surface temperatures? *Geophys. Res. Lett.*, **44**, 8520–8529, https://doi.org/10.1002/2017GL074088.

——, M. A. Alexander, and J. D. Scott, 2011a: An empirical model of tropical ocean dynamics. *Climate Dyn.*, **37**, 1823–1841, https://doi.org/10.1007/s00382-011-1034-0.

——, S.-I. Shin, and M. A. Alexander, 2011b: Natural variation in ENSO flavors. *Geophys. Res. Lett.*, **38**, L14705, https://doi.org/10.1029/2011GL047658.

Penland, C., 1996: A stochastic model of Indo-Pacific sea surface temperature anomalies. *Physica D*, **98**, 534–558, https://doi.org/10.1016/0167-2789(96)00124-8.

——, and L. Matrosova, 1994: A balance condition for stochastic numerical models with application to the El Niño–Southern Oscillation. *J. Climate*, **7**, 1352–1372, https://doi.org/10.1175/1520-0442(1994)007<1352:ABCFSN>2.0.CO;2.

——, and P. Sardeshmukh, 1995: The optimal growth of tropical sea surface temperature anomalies. *J. Climate*, **8**, 1999–2024, https://doi.org/10.1175/1520-0442(1995)008<1999:TOGOTS>2.0.CO;2.

Philander, S. G., 1983: El Niño–Southern Oscillation phenomena. *Nature*, **302**, 295–301, https://doi.org/10.1038/302295a0.

Rasmusson, E. M., and T. H. Carpenter, 1982: Variations in tropical sea surface temperature and surface wind fields associated with the Southern Oscillation/El Niño. *Mon. Wea. Rev.*, **110**, 354–384, https://doi.org/10.1175/1520-0493(1982)110<0354:VITSST>2.0.CO;2.

Rayner, N. A., D. E. Parker, E. B. Horton, C. K. Folland, L. V. Alexander, D. P. Rowell, E. C. Kent, and A. Kaplan, 2003: Global analyses of sea surface temperature, sea ice, and night marine air temperature since the late nineteenth century. *J. Geophys. Res.*, **108**, 4407, https://doi.org/10.1029/2002JD002670.

Ropelewski, C. F., and M. S. Halpert, 1987: Global and regional scale precipitation patterns associated with the El Niño/Southern Oscillation. *Mon. Wea. Rev.*, **115**, 1606–1626, https://doi.org/10.1175/1520-0493(1987)115<1606:GARSPP>2.0.CO;2.

Schopf, P. S., and M. J. Suarez, 1988: Vacillations in a coupled ocean–atmosphere model. *J. Atmos. Sci.*, **45**, 549–566, https://doi.org/10.1175/1520-0469(1988)045<0549:VIACOM>2.0.CO;2.

Shin, S. I., P. D. Sardeshmukh, M. Newman, C. Penland, and M. A. Alexander, 2021: Impact of annual cycle on ENSO variability and predictability. *J. Climate*, **34**, 171–193, https://doi.org/10.1175/JCLI-D-20-0291.1.

Smith, C. A., G. P. Compo, and D. K. Hooper, 2014: Web-Based Reanalysis Intercomparison Tools (WRIT) for analysis and comparison of reanalyses and other datasets. *Bull. Amer. Meteor. Soc.*, **95**, 1671–1678, https://doi.org/10.1175/BAMS-D-13-00192.1.

Takahashi, K., A. Montecinos, K. Goubanova, and B. Dewitte, 2011: ENSO regimes: Reinterpreting the canonical and Modoki El Niño. *Geophys. Res. Lett.*, **38**, L10704, https://doi.org/10.1029/2011GL047364.

Thomas, E. E., and D. J. Vimont, 2016: Modeling the mechanisms of linear and nonlinear ENSO responses to the Pacific meridional mode. *J. Climate*, **29**, 8745–8761, https://doi.org/10.1175/JCLI-D-16-0090.1.

——, ——, M. Newman, C. Penland, and C. Martínez-Villalobos, 2018: The role of stochastic forcing in generating ENSO diversity. *J. Climate*, **31**, 9125–9150, https://doi.org/10.1175/JCLI-D-17-0582.1.

Thompson, C. J., and D. S. Battisti, 2000: A linear stochastic dynamical model of ENSO. Part I: Model development. *J. Climate*, **13**, 2818–2832, https://doi.org/10.1175/1520-0442(2000)013<2818:ALSDMO>2.0.CO;2.

——, and ——, 2001: A linear stochastic dynamical model of ENSO. Part II: Analysis. *J. Climate*, **14**, 445–466, https://doi.org/10.1175/1520-0442(2001)014<0445:ALSDMO>2.0.CO;2.

Torrence, C., and P. J. Webster, 1998: The annual cycle of persistence in the El Nño/Southern Oscillation. *Quart. J. Roy. Meteor. Soc.*, **124**, 1985–2004, https://doi.org/10.1002/qj.49712455010.

Trenberth, K., and D. Stepaniak, 2001: Indices of El Niño evolution. *J. Climate*, **14**, 1697–1701, https://doi.org/10.1175/1520-0442(2001)014<1697:LIOENO>2.0.CO;2.

Tziperman, E., S. E. Zebiak, and M. A. Cane, 1997: Mechanisms of seasonal–ENSO interaction. *J. Atmos. Sci.*, **54**, 61–71, https://doi.org/10.1175/1520-0469(1997)054<0061:MOSEI>2.0.CO;2.

——, L. Zanna, and C. Penland, 2008: Nonnormal thermohaline circulation dynamics in a coupled ocean–atmosphere GCM. *J. Phys. Oceanogr.*, **38**, 588–604, https://doi.org/10.1175/2007JPO3769.1.

Vimont, D., 2010: Transient growth of thermodynamically coupled variations in the tropics under an equatorially symmetric mean state. *J. Climate*, **23**, 5771–5789, https://doi.org/10.1175/2010JCLI3532.1.

——, D. Battisti, and A. Hirst, 2001: Footprinting: A seasonal connection between the tropics and mid-latitudes. *Geophys. Res. Lett.*, **28**, 3923–3926, https://doi.org/10.1029/2001GL013435.

——, ——, and ——, 2003a: The seasonal footprinting mechanism in the CSIRO general circulation models. *J. Climate*, **16**, 2653–2667, https://doi.org/10.1175/1520-0442(2003)016<2653:TSFMIT>2.0.CO;2.

——, J. Wallace, and D. Battisti, 2003b: The seasonal footprinting mechanism in the Pacific: Implications for ENSO. *J. Climate*, **16**, 2668–2675, https://doi.org/10.1175/1520-0442(2003)016<2668:TSFMIT>2.0.CO;2.

——, M. A. Alexander, and M. Newman, 2014: Optimal growth of Central and East Pacific ENSO events. *Geophys. Res. Lett.*, **41**, 4027–4034, https://doi.org/10.1002/2014GL059997.

von Storch, H., G. Burger, R. Schnur, and J. S. Von Storch, 1995: Principal oscillation patterns: A review. *J. Climate*, **8**, 377–400, https://doi.org/10.1175/1520-0442(1995)008<0377:POPAR>2.0.CO;2.

Wallace, J. M., E. M. Rasmusson, T. P. Mitchell, V. E. Kousky, and E. S. Sarachik, 1998: On the structure and evolution of ENSO-related climate variability in the tropical Pacific: Lessons from TOGA. *J. Geophys. Res.*, **103**, 14241–14259, https://doi.org/10.1029/97JC02905.

Wu, R., B. P. Kirtman, and H. van den Dool, 2009: An analysis of ENSO prediction skill in the CFS retrospective forecasts. *J. Climate*, **22**, 1801–1818, https://doi.org/10.1175/2008JCLI2565.1.

Xie, R., and F. F. Jin, 2018: Two leading ENSO modes and El Niño types in the Zebiak–Cane model. *J. Climate*, **31**, 1943–1962, https://doi.org/10.1175/JCLI-D-17-0469.1.

Xie, S.-P., and S. G. H. Philander, 1994: A coupled ocean-atmosphere model of relevance to the ITCZ in the eastern Pacific. *Tellus*, **46A**, 340–350, https://doi.org/10.3402/tellusa.v46i4.15484.

You, Y., and J. C. Furtado, 2017: The role of South Pacific atmospheric variability in the development of different types of ENSO. *Geophys. Res. Lett.*, **44**, 7438–7446, https://doi.org/10.1002/2017GL073475.

Yu, J.-Y., and S. T. Kim, 2011: Relationships between extratropical sea level pressure variations and the central Pacific and eastern Pacific types of ENSO. *J. Climate*, **24**, 708–720, https://doi.org/10.1175/2010JCLI3688.1.

——, H.-Y. Kao, T. Lee, and S. T. Kim, 2011: Subsurface ocean temperature indices for Central-Pacific and Eastern-Pacific types of El Niño and La Niña events. *Theor. Appl. Climatol.*, **103**, 337–344, https://doi.org/10.1007/s00704-010-0307-6.

Zanna, L., and E. Tziperman, 2005: Nonnormal amplification of the thermohaline circulation. *J. Phys. Oceanogr.*, **35**, 1593–1605, https://doi.org/10.1175/JPO2777.1.

Zebiak, S., and M. Cane, 1987: A model El Niño–Southern Oscillation. *Mon. Wea. Rev.*, **115**, 2262–2278, https://doi.org/10.1175/1520-0493(1987)115<2262:AMENO>2.0.CO;2.

Zheng, F., and J. Y. Yu, 2017: Contrasting the skills and biases of deterministic predictions for the two types of El Niño. *Adv. Atmos. Sci.*, **34**, 1395–1403, https://doi.org/10.1007/s00376-017-6324-y.